Journal of Hazardous Materials 211–212 (2012) 95–103

Contents lists available at SciVerse ScienceDirect

Journal of Hazardous Materials

journal homepage: www.elsevier.com/locate/jhazmat

Mesoporous zinc ferrite: Synthesis, characterization, and photocatalytic activity with H_2O_2/visible light

Minhua Su[a], Chun He[a,d,*], Virender K. Sharma[b], Mudar Abou Asi[a], Dehua Xia[a], Xiang-zhong Li[c], Huiqi Deng[a], Ya Xiong[a]

[a] School of Environmental Science and Engineering, Sun Yat-sen University, Guangzhou 510275, China
[b] Chemistry Department, Florida Institute of Technology, 150 West University Boulevard, FL 32901, USA
[c] Department of Civil and Structural Engineering, The Hong Kong Polytechnic University, Hong Kong, China
[d] Guangdong Provincial Key Laboratory of Environmental Pollution Control and Remediation Technology, Guangzhou 510275, China

ARTICLE INFO

Article history:
Received 14 May 2011
Received in revised form
12 September 2011
Accepted 1 October 2011
Available online 6 October 2011

Keywords:
Mesoporous $ZnFe_2O_4$
Cationic surfactant
Hydroxyl radical
Acid Orange II

ABSTRACT

Mesoporous $ZnFe_2O_4$ (meso-$ZnFe_2O_4$) was synthesized by a hydrothermal process in which cetyltrimethylammonium bromide (CTAB) participates in the reaction to produce nanocrystals. Synthesized $ZnFe_2O_4$ was characterized by energy dispersive spectroscopy (EDS), X-ray diffraction (XRD), Brunauer–Emmett–Teller (BET) surface area, scanning electronic microscopy (SEM), transmission electron microscopy (TEM), and diffuse reflectance spectra (DRS). The meso-$ZnFe_2O_4$ was resulted from the agglomeration of nanoparticles with size of 5–10 nm. The photocatalytic activity of $ZnFe_2O_4$ under visible light ($\lambda > 400$ nm) was evaluated by the degradation of Acid Orange II (AOII) at different sintering temperatures, the amount of $ZnFe_2O_4$, and the concentration of H_2O_2. The photocatalytic degradation of AOII was almost complete within 2 h in H_2O_2/visible light system. The high efficiency for AOII degradation was attributed to the strong absorption of $ZnFe_2O_4$ in visible-light region and the generation of reactive $^{\bullet}OH$ by H_2O_2 in the system. The involvement of $^{\bullet}OH$ in oxidizing AOII was examined by determining the photocurrent of $ZnFe_2O_4$, [$^{\bullet}OH$], and degradation rates using different scavengers. Organic compounds as intermediates of the degradation process were identified by LC/MS. Moreover, $ZnFe_2O_4$ retained their degradation efficiencies for a series of repetitive batch runs, indicating the true photocatalytic process.

1. Introduction

Effective removal of reluctantly biodegraded carcinogenic azo dyestuffs primary generated from the textile, paper, food, cosmetic, and pharmaceutical industries remains a challenge in the wastewater treatment processes [1,2]. Applications of the existing conventional physical–chemical and biological techniques represent unsatisfactory outcomes because of ineffective or non-destructive mineralization of these recalcitrant compounds [3,4]. Heterogeneous photocatalysis has been widely utilized for water purification and wastewater treatment due to their promise of cost-effective technology for degrading organic pollutants [3,5]. Current exploring the highly active photocatalysts with narrow band gap which function in the visible light region has attracted a remarkable attention [6–8]. Nanosized spinel-ferrites have numerous uses including electronic, magnetic, energy, and catalytic applications [9–12]. Zinc ferrite ($ZnFe_2O_4$) is one of the most interesting ferrites due to the dependence of its magnetic behavior on particle size [13,14]. $ZnFe_2O_4$ nanoparticles have a considerable photo-response in the visible light region (1.92 eV) with good photochemical stability [15], suggesting their potential uses as gas sensors and semiconductor photocatalysts. The size of $ZnFe_2O_4$ is an important parameter with respect to properties and several synthetic methods, including co-precipitation and sol–gel techniques, have been developed [16–18]. Both of these methods usually result in large particles and a broad size distribution. A hydrothermal method has been developed which can synthesize smaller size $ZnFe_2O_4$ [19,20]. The present paper demonstrates the use of a cationic surfactant, cetyltrimethylamminium bromide (CTAB) in the hydrothermal method, for controlling the size and morphology of the synthesized nanocrystals. Various surface techniques were used to characterize $ZnFe_2O_4$, produced by this method.

Several reports on applications of the photocatalytic activity of $ZnFe_2O_4$ used in the degradation of pollutants are forthcoming [19–21]. Zinc ferrite-doped TiO_2 photocatalysts were used to degrade pollutants under UV and visible light. The current paper presents for the first time the direct application of $ZnFe_2O_4$, in combination with H_2O_2 and visible light, to the oxidation of the

* Corresponding author at: School of Environmental Science and Engineering, Sun Yat-sen University, Guangzhou 510275, China. Tel.: +86 20 39332690; fax: +86 20 39332690.
E-mail address: hechun@mail.sysu.edu.cn (C. He).

0304-3894/$ – see front matter © 2011 Elsevier B.V. All rights reserved.
doi:10.1016/j.jhazmat.2011.10.006

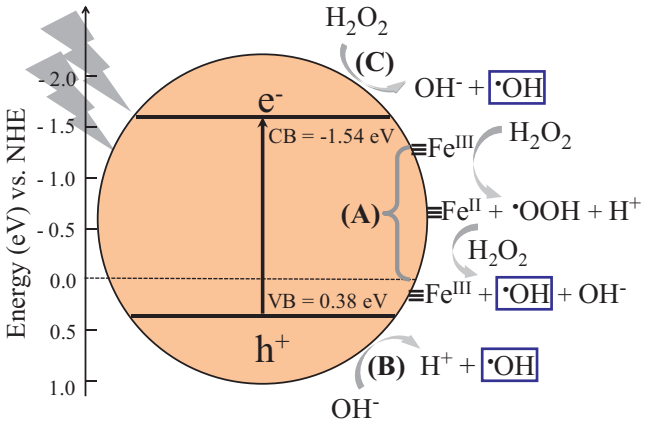

Fig. 1. A hypothetical scheme for the generation of •OH radical in H_2O_2–$ZnFe_2O_4$–visible light system.

recalcitrant organic pollutant, Acid Orange II (AOII). AOII is a good model to study because of its simpler structure than many other important recalcitrant dyes. Moreover, direct photolysis of AOII by either UV or visible light was difficult [22,23]. The potential of $ZnFe_2O_4$ to oxidize pollutants in the system is based on the hypothesis, which is presented in Fig. 1. Fe(III) on the surface of $ZnFe_2O_4$ can initiate reactions which produce •OH radical by the Fenton reaction (Path A). The valence band edge of $ZnFe_2O_4$ is located at *ca.* 0.38 eV vs. SCE while the conduction band is at −1.54 eV vs. SCE [24]. In the presence of light, holes (h_{vb}) are produced which can oxidize pollutant molecules. Holes may also oxidize water to form •OH radical (Path B). Importantly, H_2O_2 in the system can capture electrons, thus diminishing the recombination of holes and electrons, which can enhance the photocatalytic performance of $ZnFe_2O_4$ in the presence of H_2O_2 and visible light. Furthermore, the capturing of electrons produces •OH radical (Path C). The combined effects of Paths A, B, and C are thus expected to enhance the degradation of pollutants.

The objectives of this paper are to: (i) synthesize and characterize synthesized $ZnFe_2O_4$, (ii) investigate the enhanced photocatalytic activity of the $ZnFe_2O_4$–H_2O_2–visible light combination compared to either $ZnFe_2O_4$–H_2O_2 or $ZnFe_2O_4$–visible light by following the degradation of AOII in these different systems, (iii) investigate the major reactive species responsible for oxidizing AOII using various scavengers (oxalate, Cr(VI), iso-propanol, and KI) in a $ZnFe_2O_4$–H_2O_2–visible light system, (iv) provide possible pathways for the oxidation of AOII in the system by determining COD and by identifying intermediates of the reaction using LC/MS, and (v) determine the suitability of $ZnFe_2O_4$ in real world applications by checking its stability and by quantifying the extent of leaching of Zn and Fe.

2. Materials and methods

2.1. Materials

Salts of iron(III) ($Fe(NO_3)_3{\cdot}9H_2O$) and zinc(II) ($Zn(NO_3)_2{\cdot}6H_2O$) were analytical grade and were purchased from Guangdong Guanhua Chemical Co. Ltd., China. Cetyltrimethyl ammonium bromide (CTAB, $C_{16}H_{33}N^+(CH_3)_3Br^-$; purity: >98%) was obtained from the Tianjing Fuchen Chemical Reagent Co. Ltd., China. Other chemicals were analytical grade and were purchased as reagent grade. All chemicals were used without further purification. Doubly-distilled deionized water was used throughout this study.

2.2. Preparation of $ZnFe_2O_4$

$ZnFe_2O_4$ powder was prepared in the presence of CTAB by using the hydrothermal method. One gram of CTAB, as dispersant, was dissolved in 35 mL of $Zn(NO_3)_2$ solution (0.2 M) to form a homogeneous solution, which was then mixed with 35 mL of $Fe(NO_3)_3$ solution (0.4 M). The mixed solution, with a stoichiometric ratio of 1:2 ([Zn]:[Fe]), was stirred magnetically at 273 K for 30 min. Sodium hydroxide solution (6.0 M) was added slowly into the mixture to obtain a solution pH of 10.0. This solution was pretreated in an ultrasonic water bath for 30 min and then transferred into a 500 mL Teflon-lined stainless steel autoclave in order to keep it at 130 °C for 24 h in an oven. Subsequently, the autoclave was cooled to room temperature gradually. Finally, the precipitate was centrifuged and washed with deionized water several times to reduce the possibility of impurities in the products. The resulting product was dried in a vacuum oven at 75 °C for 6 h. Some of the ferrites were also obtained by drying under vacuum at 200–600 °C.

2.3. Characterization of $ZnFe_2O_4$

X-ray diffraction (XRD) analysis was conducted using a diffractometer (Bruker AXS, Germany) with radiation of Cu target (Kα, λ = 1.54059 Å). Specific BET surface area and pore size distribution were determined with an Autosorb-1-C Chemisorption/Physisorption Analyzer (Quantachrome, USA) by nitrogen adsorption at 77.3 K. The morphology of the $ZnFe_2O_4$ was analyzed with a JSM-6330F field emission scanning electron microscope (JEOL, Japan) using an acceleration voltage of 20 kV. The content of Zn and Fe in the catalyst was determined by the use of SEM–EDS–EBSD thermal field emission scanning electron microscopy (JEOL, Japan). The synthesized $ZnFe_2O_4$ was then examined by a transmission electron microscope (TEM, JEM-2010HR). The catalysts were further examined by a spectrophotometer (Shimadzu UV-PC3101PC) with an integrating sphere (Specular Reflectance ATT.5DEG) to record their diffuse reflectance spectra (DRS), in which a baseline was recorded using barium sulfate.

The photoelectrochemical measurements were performed using an IM6ex electrochemical workstation (Zahner, Germany) with a standard three-electrode assembly. This assembly had a $ZnFe_2O_4$/ITO (indium-oxide) electrode as a photoanode, a Pt wire as a cathode, and a saturated calomel electrode (SCE) as a reference electrode. To prepare $ZnFe_2O_4$/ITO electrodes, ITO plates were first cleaned by sonication in a mixture of acetone, ethanol, and deionized water for 10 min. ITO plates were coated with $ZnFe_2O_4$ slurry, containing solid polyvinylidene fluoride (PVDF) and N-methyl-2-pyrrolidone (NMP) solvent. The weighted ratio in the solid was 9:1 ($ZnFe_2O_4$:PVDF). Finally, $ZnFe_2O_4$-coated ITO plates were dried at 75 °C for 6 h to evaporate the excess NMP, yielding the $ZnFe_2O_4$/ITO electrodes. A solution of sodium sulfate (0.01 M) was adjusted to pH 6.0 and then saturated with N_2 for use as the supporting electrolyte. A 150 W middle-pressure Xenon arc lamp with filter to remove light <400 nm wavelength was used as the visible light source.

2.4. Experimental procedure

All the experiments were carried out in a cylindrical Pyrex reactor with an effective volume of 400 mL. A 150 W middle-pressure Xenon arc lamp (Shanghai Aojia Lighting Appliance Co. Ltd.), equipped with a glass jacket filled with 2 M $NaNO_2$ solution, was put inside the reactor to provide visible light irradiation (λ > 400 nm). An air flow of 100 mL min^{-1} was employed continuously to produce a fully well-dispersed suspension of $ZnFe_2O_4$ in the solution during the photoreaction. In experiments, a 400 mL solution of 100 mg L^{-1} AOII was adjusted to the desired pH of 6.0 by adding few drops of 0.01 M HCl to the solution before the

reaction, and the ferrite was suspended at a concentration of 0.5 g L^{-1}. Prior to irradiation, suspensions were sonicated at 100 W for 10 min and magnetically stirred for 30 min in the dark at room temperature to establish the adsorption/desorption equilibrium. During the reaction, samples were taken periodically using a syringe and subjected to filtration using a 0.22 μm Millipore membrane filter before measuring the UV–vis absorption spectra of solution.

2.5. Analytical methods

The concentration of AOII was analyzed by UV–vis spectroscopy (UV-2501PC, Shimadzu) at a maximum wavelength of 484 nm. Chemical oxygen demand (COD) was measured with potassium dichromate after samples were digested with a MS-3 COD microwave digestion system according to the standard method. Prior to COD analysis, residual H_2O_2 was removed by the addition of MnO_2 at pH 9.0 to eliminate interference with analytical measurements [25]. The concentrations of leached Fe and Zn in the solution were measured by Inductively Coupled Plasma Optical Emission Spectrometry (ICP-OES, optima 5300DV, Perkin-Elmer).

The intermediates of AOII oxidation were analyzed by liquid chromatography–mass spectrometry (LC–MS, Agilent 1100 LC, equipped with a Model 486 variable wave wavelength UV detector set at 256 nm). A zorbax eclipse XDB C8 column 150 mm × 4.6 mm was used for separating product intermediates. The mobile phase was a filtered mixture of acetonitrile and 0.1 M ammonium acetate. The flow rate was 1 mL min^{-1}. From 0 to 5 min, the ratio of acetonitrile:ammonium acetate was 1:1; from 5 to 10 min the ratio was 2:1. The injection volume was 10 μL. MS analysis in the positive and negative ion mode was performed using a mass spectrometer equipped with an ESI ion source. The ESI probe tip and capillary potentials were set at 3.0 kV and 18 V, respectively. The mass range was 120–500 *m*/*z*. The heated capillary was set to 250 °C.

The concentration of •OH was determined according to the method reported earlier [26,27]. Briefly, benzene was used as a probe to determine the photoproduction of •OH for the formation of phenol from the reaction of benzene with •OH ($k = 5.9 \times 10^9$ M^{-1} s^{-1}) in aqueous solution [28], in which •OH-mediated oxidation of benzene forms phenol and the concentration of phenol represented the amount of •OH photoproduction [26]. In this experimental set-up, a 400 mL benzene solution (10 mM) and 0.5 g L^{-1} $ZnFe_2O_4$ were mixed thoroughly and transferred into the photoreactor. Different concentrations of H_2O_2 were added into the aqueous solution, which was irradiated for 30 min using the same xenon arc lamp. The control experiments without $ZnFe_2O_4$, in the dark, were carried out in parallel. After the reaction, the samples were separated from $ZnFe_2O_4$ suspension. The concentrations of phenol were determined using the 4-aminoantipyrine spectrophotometric method [27].

3. Results and discussion

3.1. Characterization of $ZnFe_2O_4$

The result of EDS analysis, shown in Fig. 2a, indicates the presence of Zn, Fe, and O elements in $ZnFe_2O_4$ powder. The determined atomic ratio of Zn to Fe in the powder was 1:2.03, which is in close proximity to the theoretical ratio in $ZnFe_2O_4$. The $ZnFe_2O_4$ powder, prepared at different sintered temperatures, was also analyzed by XRD (Fig. 2b). XRD patterns showed that $ZnFe_2O_4$ had cubic spinel structures, which is consistent with the values reported in the database of $ZnFe_2O_4$ (JCPDS 22-1012). The peak intensity gradually increased with the increase in sintering temperature. The TEM image showed that the as-prepared $ZnFe_2O_4$ had a typical

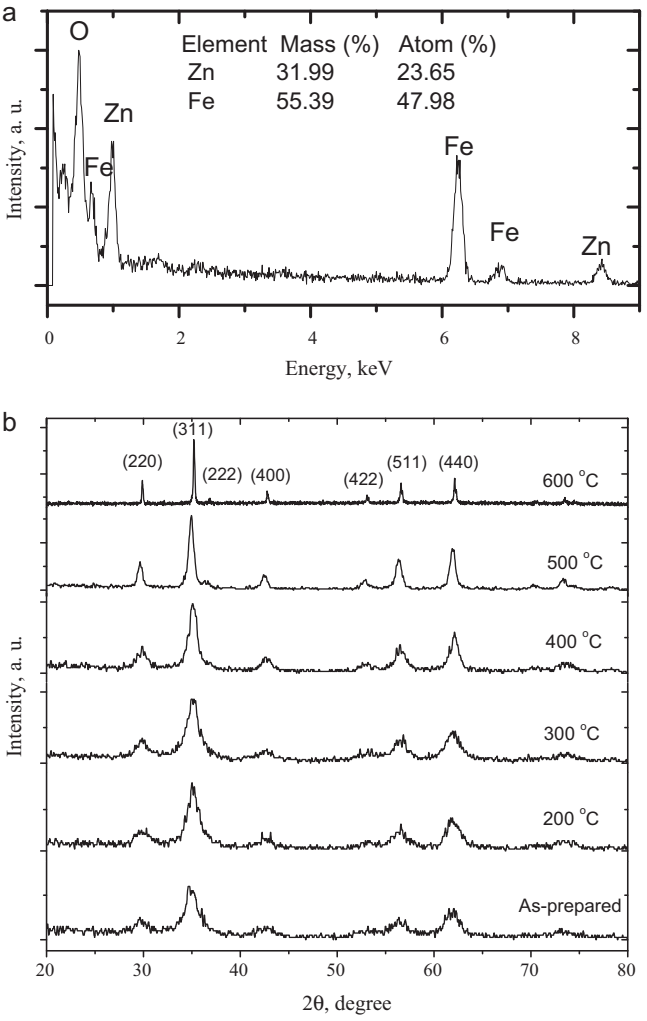

Fig. 2. EDS spectrum (a) and XRD patterns (b) of $ZnFe_2O_4$.

mesostructure with a wormhole framework (Fig. 3a). Apparently, the agglomeration of nanoparticles with size of 5–10 nm resulted in the mesostructure of $ZnFe_2O_4$. An HRTEM analysis indicates that the lattice spacing is 0.299 nm for the (2 2 0) plane, which clearly demonstrates the crystal structure of $ZnFe_2O_4$ (inset of Fig. 3a).

Significantly, the use of CTAB in the synthesis of $ZnFe_2O_4$ decreased the particles size (Fig. S1). Particle sizes were 5–10 nm and 80 nm with and without CTAB in the synthesis procedure (Fig. S1). This suggests that the cationic surfactant had a significant role in inhibiting the growth of the crystals, which led to the uniformly of the nano-sized catalyst. The following steps may explain the participation of CTAB in the synthesis of meso-$ZnFe_2O_4$.

$$\text{Hydrolysis}: \text{CTAB} \rightarrow \text{CTA}^+ + \text{Br}^- \quad (1)$$

$$\text{Precipitation}: \text{Zn}^{2+} + \text{Fe}^{3+} + \text{OH}^- \rightarrow \text{Zn-Fe-OH}^- \quad (2)$$

$$\text{Electrostaticinteraction}: \text{CTA}^+ + \text{Zn-Fe-OH}^- \rightarrow \text{CTA-OH-Fe-Zn} \quad (3)$$

$$\text{Hydrothermalstep}: \text{CTA-OH-Fe-Zn} \rightarrow \text{ZnFe}_2\text{O}_4 \quad (4)$$

CTAB in aqueous solution ionizes to CTA^+ and Br^- (Eq. (1)). In excess amounts of dissolved NaOH, the mixture of $Zn(NO_3)_2$ and $Fe(NO_3)_3$ solutions forms Zn-Fe-OH^- (Eq. (2)). The electrostatic interaction between CTA^+ and Zn-Fe-OH^- form CTA-OH-Fe-Zn (Eq. (3)), which acts as a precursor for the formation of meso-$ZnFe_2O_4$ crystals in

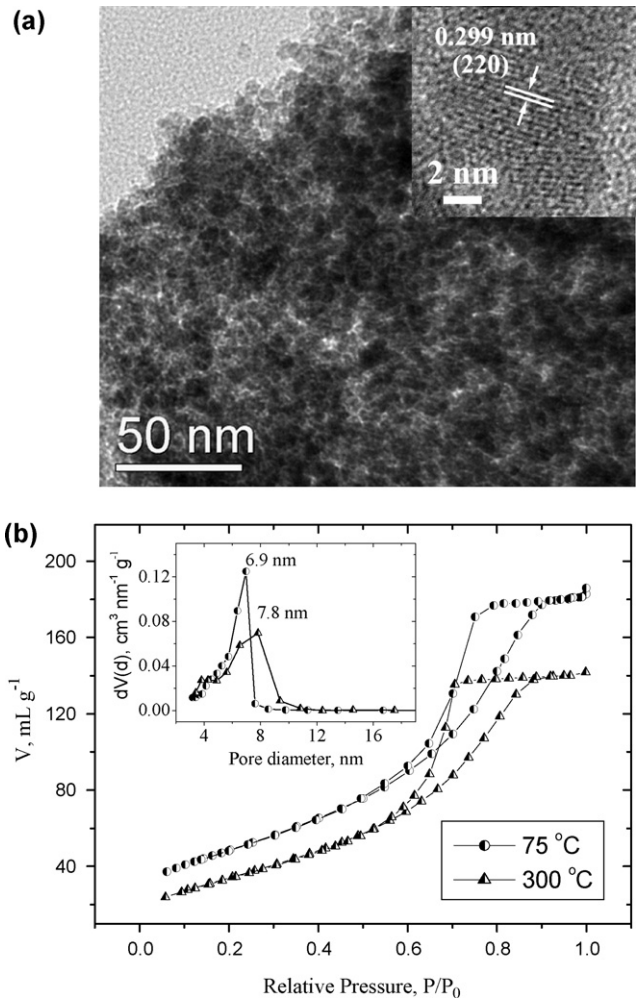

Fig. 3. (a) TEM and HRTEM (inset) images of meso-$ZnFe_2O_4$ and (b) nitrogen adsorption/desorption isotherms and pore size distribution (inset) of meso-$ZnFe_2O_4$.

the hydrothermal process (Eq. (4)). With an increase of sintering temperature from 300 to 500 °C, the size of the particles increased from *ca.* 30 to 100 nm (Fig. S1c–e), and a significant aggregation of the particles occurred at 500 °C. When the sintering temperature was set to 600 °C, the particles size increased again (Fig. S1f), possibly due to aggregation.

Nitrogen adsorption–desorption studies on as-prepared meso-$ZnFe_2O_4$ showed a type IV isotherm with an inflection of nitrogen adsorbed volume at P/P_0 about 0.5, indicating a typical of mesoporous materials (Fig. 3b). The specific surface area, calculated from the linear region of the Brunauer–Emmett–Teller (BET) plot, was 175.4 $m^2\,g^{-1}$, and the pore diameter, calculated from the nitrogen adsorption isotherm by the Barrett–Joyner–Halenda (BJH) method, was 6.9 nm. The BET surface area and pore diameter of $ZnFe_2O_4$ for sintering temperatures of 300 °C were 132.3 $m^2\,g^{-1}$ and 7.8 nm, respectively. These data suggested that the BET surface area of $ZnFe_2O_4$ decreased with the increase of thermal treatment temperature. The measured BET surface areas of $ZnFe_2O_4$ were 175.4, 153.1, 132.3, 107.6, 67.4, and 25.9 $m^2\,g^{-1}$ for sintering temperatures of 75, 200, 300, 400, 500, and 600 °C, respectively. The photocatalytic activity of the prepared $ZnFe_2O_4$ at high sintering temperatures is thus expected to be low, due to the decreased specific surface area of the larger particles.

The meso-$ZnFe_2O_4$ was analyzed by UV–vis absorption spectroscopy to investigate the optical properties (Fig. 4). The meso-$ZnFe_2O_4$ was found to absorb visible light more efficiently

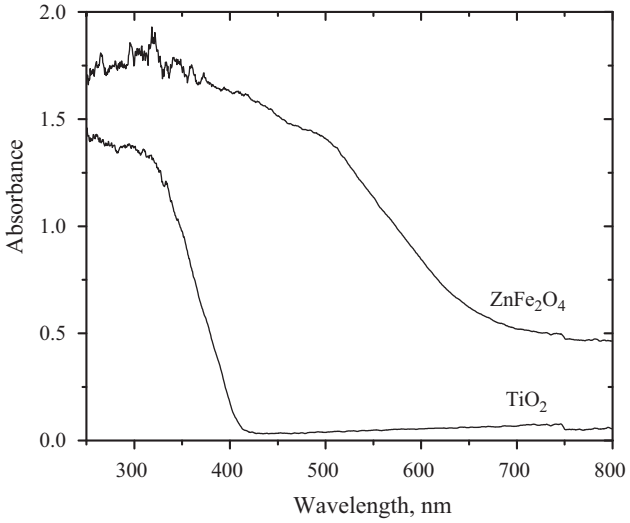

Fig. 4. UV–vis DRS of meso-$ZnFe_2O_4$ and TiO_2.

than photocatalytic TiO_2 nanoparticles. The absorption results demonstrate that $ZnFe_2O_4$ has significant absorbance in the 450–700 nm wavelength range, which is important for performing photocatalytic reactions under visible light. The absorption shoulder of the ferrite in the visible region may be attributed to the electron excitation from the O-2p level into the Fe 3d level for spinel-type compound [29]. The band gap of meso-$ZnFe_2O_4$, calculated from the plot of the transformed Kubelka–Munch function vs. the energy of light, is 1.92 eV (646 nm). Comparatively, the absorption edge of TiO_2 (Degussa P25) is 3.06 ev (405 nm).

3.2. Photocatalytic activity of $ZnFe_2O_4$

The photocatalytic activity of $ZnFe_2O_4$ powder under visible light was evaluated by performing experiments on the degradation of AOII in aqueous solution under various conditions. First, the performance of the ferrite, synthesized at different sintering temperatures, was tested (Fig. S2a). The degradation of AOII followed the pseudo first-order kinetics for more than 90% completion of the reaction. The kinetics may be expressed as

$$\ln\left(\frac{C_0}{C}\right) = k't \tag{5}$$

where k' is the apparent reaction constant and C_0 and C are the initial concentration and the concentration at time t, of AOII, respectively.

Fig. 5a shows the values of k' for different sintering temperatures of ferrite synthesis, which were of the order of $10^{-3}\,min^{-1}$. Results showed no significant difference in k' in the sintering temperature range of 75–300 °C, followed by a gradual decrease with increase in temperature. The decrease in the catalytic activity of $ZnFe_2O_4$ could be attributed to the significant decrease in specific surface area of the larger particles. This is supported by the experimentally observed results of BET surface area measurement of $ZnFe_2O_4$ (see previous section). A decrease in the photocatalytic activity of $ZnFe_2O_4$ with increase in sintering temperature for the degradation of methyl orange under UV-light irradiation was also observed [18]. Therefore, the sintering process of $ZnFe_2O_4$ should be maintained at a relatively low temperature. Experiments in the present study were therefore performed using ferrite synthesized at the lowest temperature of 75 °C.

Next, the effect of the amount of meso-$ZnFe_2O_4$ on the degradation of AOII was investigated (Fig. S2b). The values of k' for the degradation of AOII increased from $2.5 \times 10^{-3}\,min^{-1}$ to

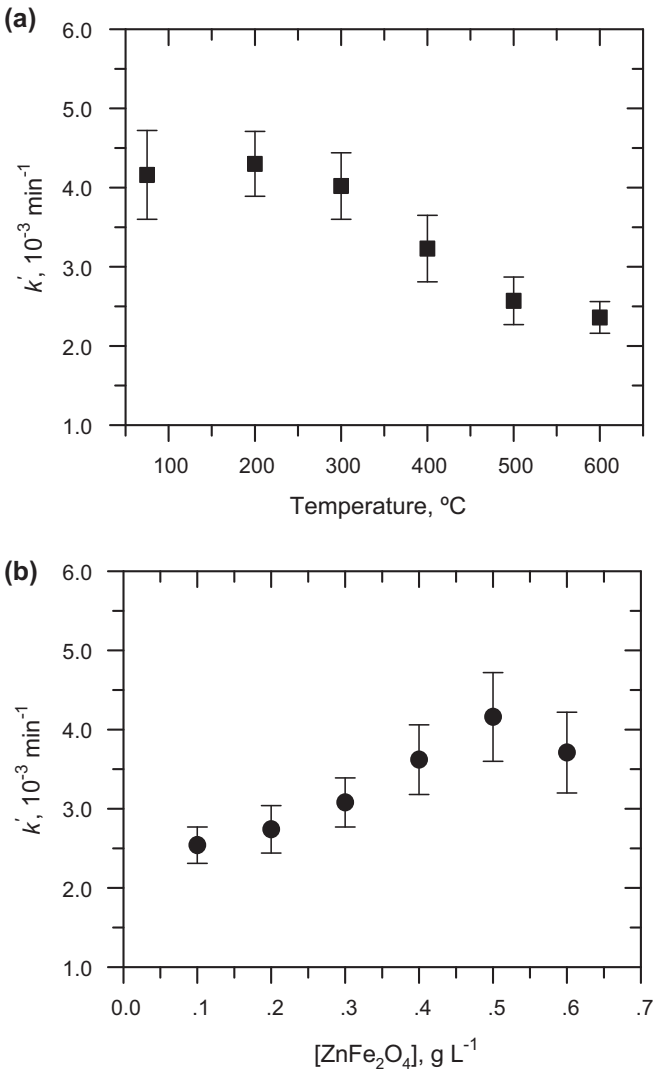

Fig. 5. Values of k' for the degradation of AOII by ferrite sintered at different temperatures (a) and on the amount of prepared $ZnFe_2O_4$ at 75 °C (b) (reaction conditions: initial AOII concentration = 100 mg L^{-1} and initial solution pH = 6.0).

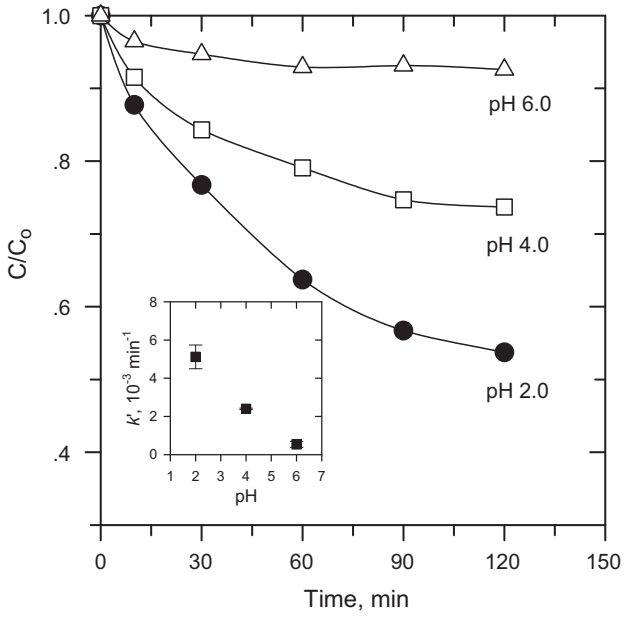

Fig. 6. Effect of pH on the degradation of AOII without visible light (reaction conditions: initial AOII concentration = 100 mg L^{-1}, $ZnFe_2O_4$ suspension = 0.5 g L^{-1}, and initial H_2O_2 concentration = 12.0 mM).

4.0×10^{-3} min^{-1} in varying the amount of ferrite from 0.1 to 0.5 g L^{-1} (Fig. 5b). No further increase in k' was observed with increase in the amount of ferrite in solution (Fig. 5b). A high concentration of suspended $ZnFe_2O_4$ may block the visible light to some extent hindering ability to achieve the full capacity of the process of degradation under visible light. Further experiments were therefore conducted using 0.5 g L^{-1} $ZnFe_2O_4$ in the reaction solution.

Finally, the role of H_2O_2 in the degradation of AOII with and without light was explored. The experiments without visible light were carried out at different pH (2.0–6.0) (Fig. 6). The value of k' varied from 0.53×10^{-3} at pH 6.0 to 5.1×10^{-3} min^{-1} at pH 2.0. This decrease in rate with increase in pH clearly demonstrates the possible role of the Fenton reaction, which occurred favorably at low pH to generate •OH, a likely species to degrade AOII. However, experiments in the presence of light were conducted at pH 6.0 because of the desirability of degrading AOII at pH values close to the neutral conditions. It should be pointed out that besides participation of the Fenton reaction, other phenomena may also be involved, which include catalyst bands dependence on pH and change in the dye redox potential and the solid surface electrical charge with pH.

In visible light, a decrease in the concentration of AOII without H_2O_2 in the reaction system was ~40% in 120 min (Fig. 7). However, complete degradation of AOII occurred at H_2O_2 concentration of ≥7.5 mM for the same time period. The values of k' for the degradation of AOII increased with the increase of H_2O_2 concentration up to 12.0 mM, and then decreased at 15.0 mM. Significantly, the values of k' were of the order of 10^{-2} min^{-1}, which are much higher than k' values obtained in conducting experiments in either meso-$ZnFe_2O_4$/H_2O_2 or meso-$ZnFe_2O_4$/visible light. The increase in the degradation of AOII in the presence of both light and H_2O_2 may be ascribed to the formation of more •OH from the activation of H_2O_2 with $ZnFe_2O_4$ (Fig. 1). The slight decrease of AOII removal efficiency at 15 mM may be due to the scavenging of •OH by competing reactions with H_2O_2 and •OOH at higher concentration of H_2O_2 ($^{\bullet}OH + H_2O_2 \rightarrow H_2O + {}^{\bullet}OOH$ and $^{\bullet}OH + {}^{\bullet}OOH \rightarrow H_2O + O_2$) [30]. The concentration of H_2O_2 was thus kept at 12 mM to obtain maximum degradation efficiency in the present study.

3.3. Mechanism

Initially, the production of photogenerated electrons by $ZnFe_2O_4$ under visible light was tested by carrying out photocurrent–time profiles of the meso-$ZnFe_2O_4$ electrode (Fig. 8). The electrode demonstrated a rapid photocurrent response when the ferrite nanocrystals were illuminated with visible light and was maintained at constant levels within a couple of pulses. Significantly, the photocurrent of the meso-$ZnFe_2O_4$ electrode decreased in the presence of H_2O_2. This decrease may be related to the capturing of some electrons by H_2O_2 to yield hydroxyl radicals (Path C, Fig. 1) [31], which would be an advantage of the use of $ZnFe_2O_4$ photocatalyst in the presence of H_2O_2 to degrade azo dye under visible light.

The concentrations of •OH were determined in solutions under various conditions to clarify the catalytic mechanism of a possible synergistic effect of the H_2O_2-assisted $ZnFe_2O_4$ system under visible light (Fig. 9). It can be seen that no •OH was generated by either $ZnFe_2O_4$ or H_2O_2 in the dark (Bars A and C in Fig. 9). However, a small amount of •OH was produced by $ZnFe_2O_4$–H_2O_2 in the dark (Bar E in Fig. 9). Significant amounts of •OH were generated by either H_2O_2 or ferrite under visible light irradiation (Bars D and B in Fig. 9), due to the decomposition of H_2O_2 to •OH under

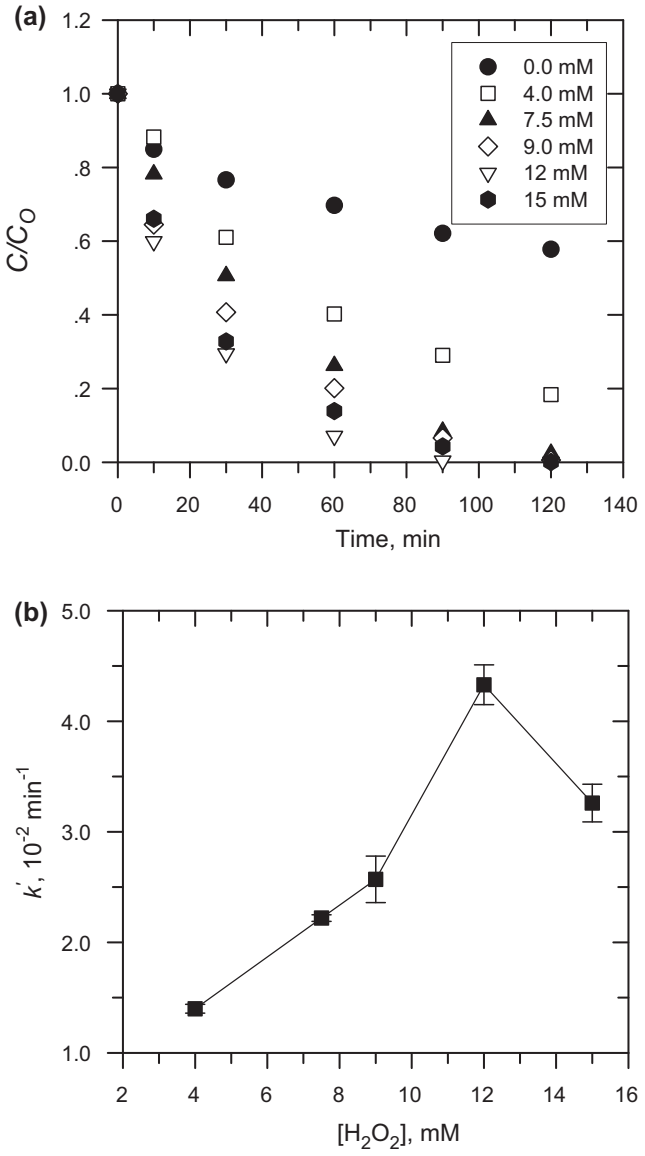

Fig. 7. (a) Effect of concentration of H_2O_2 on the degradation of AOII under visible light, and (b) values of k' as a function of the concentration of H_2O_2 (reaction conditions: initial AOII concentration = 100 mg L^{-1}, $ZnFe_2O_4$ suspension = 0.5 g L^{-1}, and initial solution pH = 6.0).

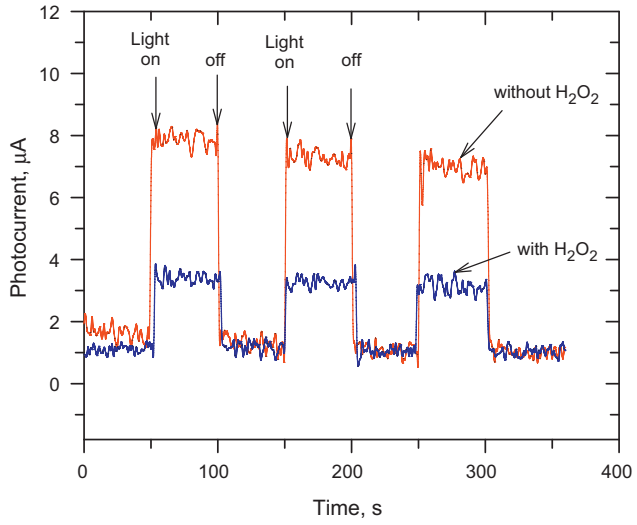

Fig. 8. Photocurrent generation on meso-$ZnFe_2O_4$/ITO electrode under visible light.

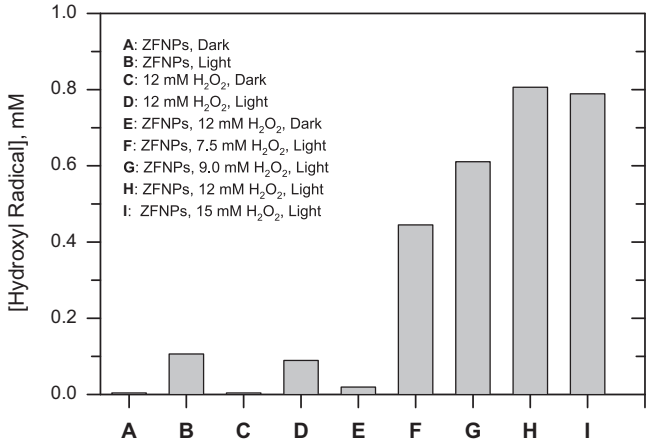

Fig. 9. Concentration of •OH radical generated at various reaction processes (reaction conditions: initial benzene concentration = 10 mM, meso-$ZnFe_2O_4$ suspension = 0.5 g L^{-1}, and initial solution pH = 6.0).

visible light (420 nm < λ < 550 nm) [32] and the oxidation of OH^- by the photogenerated holes. However, production of •OH was significantly increased in the presence of H_2O_2 and $ZnFe_2O_4$ under visible light and was dependent on the concentration of H_2O_2 (Bars F and H in Fig. 9). A slight decrease in the concentration of •OH when using 15.0 mM H_2O_2 was observed (Bar I in Fig. 9). Excess H_2O_2 may react with some of the produced •OH radicals to decrease its concentration. Therefore, it was concluded that the enhanced catalytic activity for AOII in the H_2O_2-assisted meso-$ZnFe_2O_4$ system under visible light irradiation was related to the significant increase of •OH concentration.

To further confirm the •OH radical was the reactive species mostly responsible for degradation of AOII in the H_2O_2–$ZnFe_2O_4$–visible system, several scavengers were tested in the reaction solution (Fig. 10). Oxalate has a relatively weak reactivity with •OH ($k = 4.7 \times 10^7$ M^{-1} s^{-1}), but can be oxidized easily by h_{vb}^+ [33]. The degradation efficiency of AOII with the addition of sodium oxalate was similar to that without any scavenger, indicating that the h_{vb}^+ played not much role in the oxidative reaction

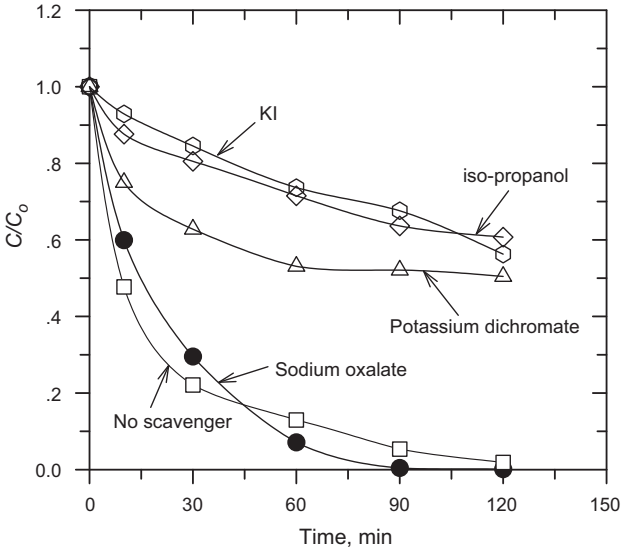

Fig. 10. Effect of scavengers on AOII degradation in meso-$ZnFe_2O_4$/H_2O_2 system under visible light (reaction conditions: AOII concentration = 100 mg L^{-1}, initial H_2O_2 concentration = 12.0 mM, meso-$ZnFe_2O_4$ suspension = 0.5 g L^{-1}, and initial solution pH = 6.0 (scavenger concentration: KI = 10 mmol L^{-1}, sodium oxalate = 10 mmol L^{-1}, iso-propanol = 10 mmol L^{-1} and Cr(VI) = 0.5 mmol L^{-1}).

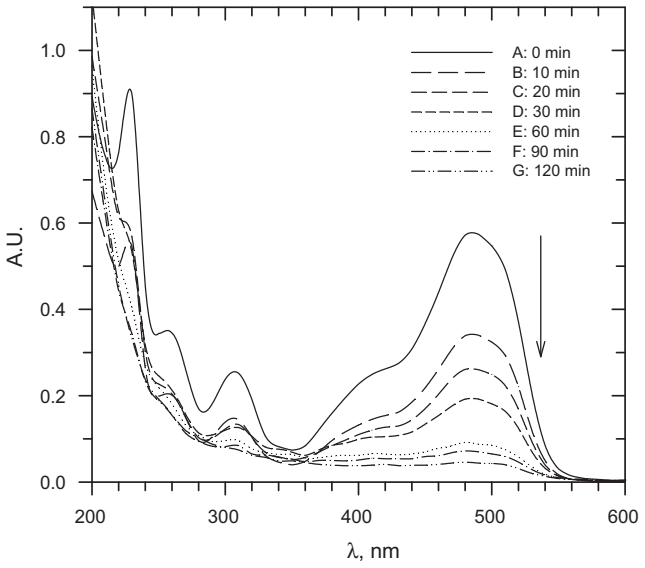

Fig. 11. UV–vis spectral change of AOII with reaction time in the H_2O_2–$ZnFe_2O_4$ system under visible light (reaction conditions: AOII concentration = 100 mg L^{-1}, initial H_2O_2 concentration = 12.0 mM, $ZnFe_2O_4$ suspension = 0.5 g L^{-1}, and initial solution pH = 6.0).

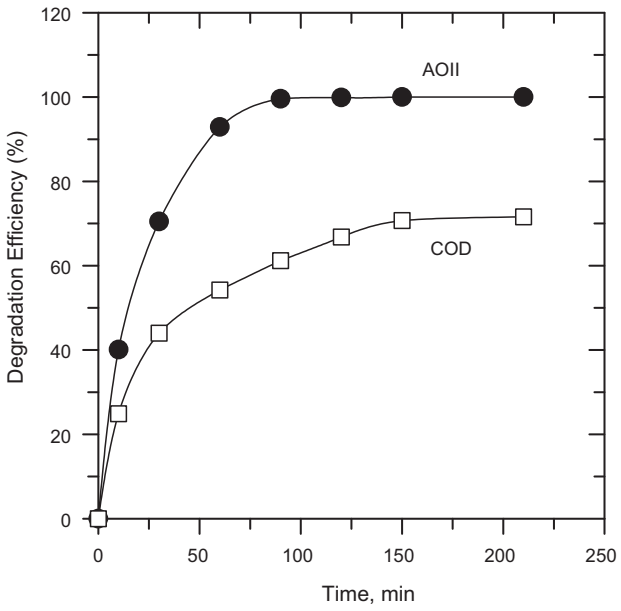

Fig. 12. Efficiency of AOII and COD removal in H_2O_2-assisted meso-$ZnFe_2O_4$ system under visible light irradiation (reaction conditions: AOII concentration = 100 mg L^{-1}, initial H_2O_2 concentration = 12.0 mM, meso-$ZnFe_2O_4$ suspension = 0.5 g L^{-1}, and initial solution pH = 6.0).

and •OH mainly contributed to the degradation of AOII in this system. Cr(VI) was used as an electron scavenger because the redox potential of Cr(VI) ($E^0(Cr_2O_7^{2-}/Cr^{3+})$ = +1.232 V vs. SCE) is more positive than that of H_2O_2 ($E^0(H_2O_{2aq}/{}^{\bullet}OH_{aq})$ = +0.38 V vs. SCE) [30,34]. As can be seen in Fig. 10, the degradation efficiency of AOII was significantly decreased with the addition of Cr(VI) because of the capturing of photogenerated electrons by Cr(VI), which led to a decrease in the concentration of •OH radicals (Path C, Fig. 1). This caused the decrease in degradation of AOII. Iso-propanol is a good scavenger for •OH ($k = 1.9 \times 10^9\ M^{-1}\ s^{-1}$) [28] while KI can scavenge rapidly both h_{vb}^+ and •OH ($k \sim 1 \times 10^{10}\ M^{-1}\ s^{-1}$) [35]. The degradation efficiency of AOII was significantly decreased with the addition of either iso-propanol or KI. Formation of other oxidizing species, $O_2^{\bullet-}$ in the reaction system, to oxidize AOII was less likely. The conduction band edge of $ZnFe_2O_4$ is at *ca.* −1.54 eV vs. SCE [24], therefore, the conduction band electron would likely be captured by H_2O_2 (E^0 ($H_2O_{2aq}/{}^{\bullet}OH_{aq}$) = +0.38 V vs. SCE) rather than by O_2 (E^0 ($O_2/{}^{\bullet}O_2^-$) = −0.33 V vs. SCE) to produce •OH (Fig. 1). Hence, the enhanced catalytic activity in the H_2O_2–$ZnFe_2O_4$ system under visible light could possibly be ascribed to the generated active •OH produced from Paths A, B, and C of Fig. 1.

3.4. Possible pathways for degradation of AOII

The degradation of AOII was followed by monitoring the UV–vis spectral changes of AOII as a function of the reaction time in the H_2O_2–$ZnFe_2O_4$ system under visible light (Fig. 11). The azo bond at 484 nm of Acid Orange II decreased with the progress of the reaction. A concomitant increase in absorbance in the wavelength range of 330–360 nm was also observed. The color of the reaction solution changed from orange to deep red after completion of the reaction. The color alteration suggests hyperchromicity in wavelengths longer than 484 nm. Overall, the results suggest that the formation of several intermediates rather than instantaneous mineralization of AOII to CO_2.

The intermediates may have no absorption at the selected wavelengths, but COD levels in the reaction solution can be used to demonstrate the presence of organics in solution. Therefore, the efficiencies of AOII and COD removals were simultaneously monitored during the degradation of AOII in the H_2O_2–$ZnFe_2O_4$–visible light system. It can be seen that the COD removal efficiency was ~67% after 120 min and the maximum COD removal efficiency was 72% after 210 min (Fig. 12). It is very clear that the COD removal efficiency was lower than the degradation efficiency (by *ca.* 30%) within the studied reaction period. These results further indicate that AOII was oxidized *via* a number of intermediates prior to its final product, CO_2, and that some intermediates also degraded, but at lower reaction rates than the degradation rate for AOII.

The identification of the intermediates in the degradation of AOII in the meso-$ZnFe_2O_4$/H_2O_2 system under visible light was performed. The identified intermediates and their main fragments as determined by LC/MS are illustrated in Table S1. Formed intermediate products for the degradation of AOII in the meso-$ZnFe_2O_4$/H_2O_2 system were 4-amino-benzenesulfonate (product A), 1-amino-naphthalen-2-ol (product B) [36], 1-amino-2-naphthoquinone (product C), 4-hydroxybenzenesulfonate (product D), cyclopenta-2,4-diene-1-sulfonate (product E), naphthalene-1,2-diol (product F), hydroquinone (product G), cyclopenta-2,4-dienol (product H), 2-hydroxy-1,4-naphthaquinone (product I), 1,2-naphthaquinone (product J). Based on the degradation products identified, a possible pathway for degradation of AOII in $ZnFe_2O_4$/H_2O_2 system is proposed in Fig. 13. The process of AOII degradation was initiated by the attack of •OH radicals through the cleavage of the azo bond at the first step to yield products A and B, leading to the apparent decolorization of AOII [37,38]. The oxidation of the benzene ring in product A, led to the formation of products D and E. The intermediate products, D and E, were further oxidized to form the polyhydroxylated intermediates (products G and H). The oxidation of intermediate product B with its equilibrium product C was responsible for the formation of product F. Subsequently, the phenolic hydroxy group in product F was further oxidized to quinoid intermediates (products I and J). Polyhydroxylated and quinoid structure intermediates would not be stable and most likely formed short-chain carboxylic acids by oxidative ring opening reactions. The short-chain carboxylic acids were finally mineralized to CO_2 and H_2O.

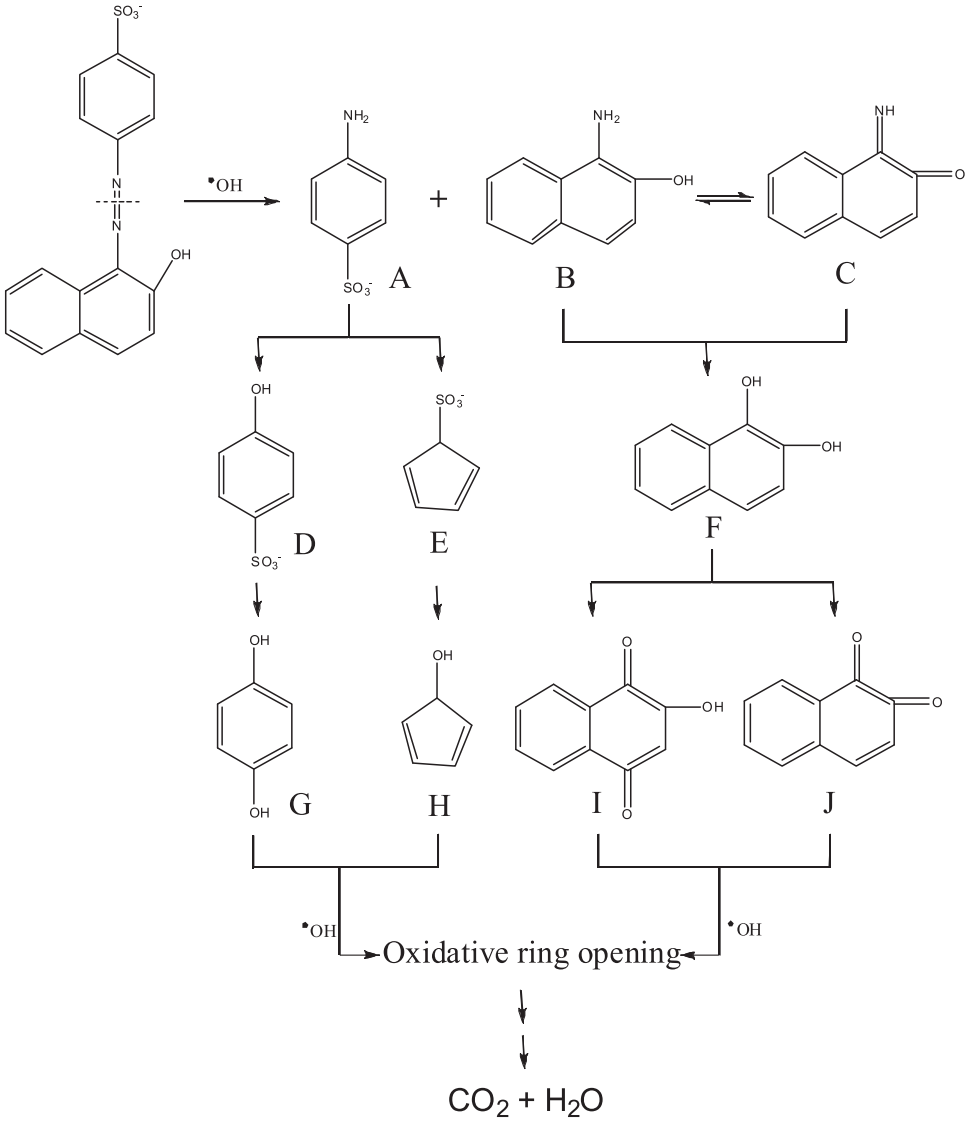

Fig. 13. A possible pathway for oxidation of AOII in H_2O_2–$ZnFe_2O_4$–visible light system.

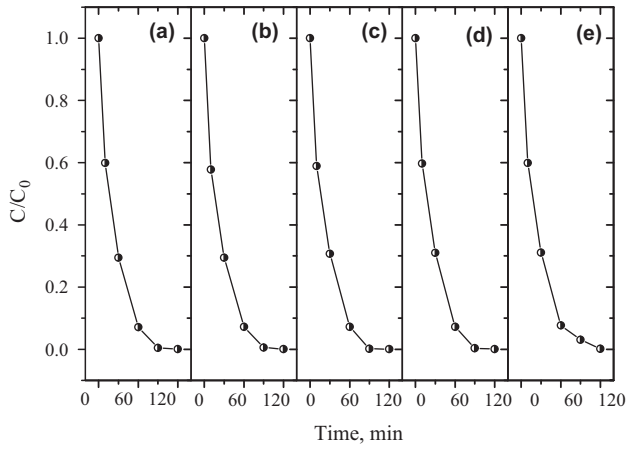

Fig. 14. Degradation of AOII in different batch runs in the H_2O_2–$ZnFe_2O_4$–visible light system. (a) First use, (b) second use, (c) third use, (d) fourth use, and (e) fifth use (reaction conditions: AOII concentration = 100 mg L^{-1}, initial H_2O_2 concentration = 12.0 mM, $ZnFe_2O_4$ suspension = 0.5 g L^{-1}, and initial solution pH = 6.0).

3.5. Stability of $ZnFe_2O_4/H_2O_2$ system

The durability and chemical stability of meso-$ZnFe_2O_4$ was tested for practical applications of the meso-$ZnFe_2O_4/H_2O_2$ system under visible light to degrade pollutants. The meso-$ZnFe_2O_4$ catalyst was repeatedly applied to degrade AOII under visible light in successive batch runs (Fig. 14). It was found that the $ZnFe_2O_4$ almost retained its catalytic activity intact after the fifth repeat in which k' was estimated to be 4.3×10^{-2} min^{-1}; similar to the k' obtained using fresh $ZnFe_2O_4$ ($k' = 4.4 \times 10^{-2}$ min^{-1}). This indicates that meso-$ZnFe_2O_4$ possesses chemical and catalytic stability (Fig. 14). Concentrations of leached Fe and Zn in solutions were measured after the degradation of AOII at pH 6.0 to determine the stability of $ZnFe_2O_4$ in aqueous solution. The concentrations of leached Fe and Zn were 0.13 and 0.63 mg L^{-1}, respectively, which suggests that no harmful effects would result from the use of the H_2O_2–$ZnFe_2O_4$–visible light system at pH 6.0 for the degradation of AOII.

4. Conclusions

The cationic surfactant CTAB in the hydrothermal synthesis used in this study played a significant role in obtaining the

meso-$ZnFe_2O_4$ resulted from the aggregation of nanoparticles with a size of 5–10 nm. The photocatalytic degradation of AOII in the H_2O_2–$ZnFe_2O_4$–visible light system followed pseudo first-order kinetics. The degradation rates for the system were much higher than those obtained in either $ZnFe_2O_4$–H_2O_2 or $ZnFe_2O_4$–visible light. The determined concentrations of •OH and degradation rates using different scavengers of e_{cb}^-, h_{vb}^+, and •OH demonstrated that the •OH radical was the reactive species responsible for the degradation of AOII in the H_2O_2–$ZnFe_2O_4$–visible light system. Ferrite maintained its degradation efficiency and durability in five repeated batch runs at pH 6.0. The released amounts of Fe and Zn after the use of ferrite at pH 6.0 were found to be low ($\leq$0.63 mg L^{-1}). The potential of meso-$ZnFe_2O_4$ as a high-performance catalyst in presence of H_2O_2 under visible light to oxidize recalcitrant organic materials was successfully demonstrated.

Acknowledgements

The authors wish to thank the National Natural Science Foundation of China (No. 20877025), the National Natural Science Foundation of Guangdong Province (No. S2011010001836), the Fundamental Research Funds for the Central Universities (No. 09lgpy20), Project from Guangzhou City (2010Z2-C1009) and Ministry of Science and Technology of China (No. 10C26214414753), and the Research Fund Program of Guangdong Provincial Key Laboratory of Environmental Pollution Control and Remediation Technology (No. 2011K0003) for financially supporting this work. V.K. Sharma would like to thank Center of Ferrate Excellence, FIT, USA. Authors wish to thank Professor Mary Sohn for useful comments.

Appendix A. Supplementary data

Supplementary data associated with this article can be found, in the online version, at doi:10.1016/j.jhazmat.2011.10.006.

References

[1] A.Z. Bouyakoub, B.S. Lartiges, R. Ouhib, S. Kacha, A.G. El Samrani, J. Ghanbaja, O. Barres, $MnCl_2$ and $MgCl_2$ for the removal of reactive dye Levafix Brilliant Blue EBRA from synthetic textile wastewaters: an adsorption/aggregation mechanism, J. Hazard. Mater. 187 (2011) 264–273.
[2] F.I. Hai, K. Yamamoto, F. Nakajima, K. Fukushi, Bioaugmented membrane bioreactor (MBR) with a GAC-packed zone for high rate textile wastewater treatment, Water Res. 45 (2011) 2199–2206.
[3] M.G. Coelho, G.M. de Lima, R. Augusti, D.A. Maria, J.D. Ardisson, New materials for photocatalytic degradation of indigo carmine-synthesis, characterization and catalytic experiments of nanometric tin dioxide-based composites, Appl. Catal. B: Environ. 96 (2010) 67–71.
[4] C.H. Huang, K.P. Chang, H.D. Ou, Y.C. Chiang, E.E. Chang, C.F. Wang, Characterization and application of Ti-containing mesoporous silica for dye removal with synergistic effect of coupled adsorption and photocatalytic oxidation, J. Hazard. Mater. 186 (2011) 1174–1182.
[5] K. Shankar, J.I. Basham, N.K. Allam, O.K. Varghese, G.K. Mor, X. Feng, M. Paulose, J.A. Seabold, K.-S. Choi, C.A. Grimes, Recent advances in the use of TiO_2 nanotube and nanowire arrays for oxidative photoelectrochemistry, J. Phys. Chem. C 113 (2009) 6327–6359.
[6] J. Kim, C.W. Lee, W. Choi, Platinized WO_3 as an environmental photocatalyst that generates OH radicals under visible light, Environ. Sci. Technol. 44 (2010) 6849–6854.
[7] W. Liu, M.S. Ji, S.F. Chen, Preparation, characterization and activity evaluation of $Ag_2Mo_4O_{13}$ photocatalyst, J. Hazard. Mater. 186 (2011) 2001–2008.
[8] G. Kim, W. Choi, Charge–transfer surface complex of EDTA–TiO_2 and its effect on photocatalysis under visible light, Appl. Catal. B: Environ. 100 (2010) 77–83.
[9] P. Laokul, V. Amornkitbamrung, S. Seraphin, S. Maensiri, Characterization and magnetic properties of nanocrystalline $CuFe_2O_4$, $NiFe_2O_4$, $ZnFe_2O_4$ powders prepared by the Aloe vera extract solution, Curr. Appl. Phys. 11 (2011) 101–108.
[10] V. Blanco-Gutierrez, M.J. Torralvo-Fernandez, R. Saez-Puche, Magnetic behavior of $ZnFe_2O_4$ nanoparticles: effects of a solid matrix and the particle size, J. Phys. Chem. C 114 (2010) 1789–1795.
[11] Y.B. Li, R. Yi, A.G. Yan, L.W. Deng, K.C. Zhou, X.H. Liu, Facile synthesis and properties of $ZnFe_2O_4$ and $ZnFe_2O_4$/polypyrrole core–shell nanoparticles, Solid State Sci. 11 (2009) 1319–1324.
[12] M. Sivakumar, T. Takami, H. Ikuta, A. Towata, K. Yasui, T. Tuziuti, T. Kozuka, D. Bhattacharya, Y. Iida, Fabrication of zinc ferrite nanocrystals by sonochemical emulsification and evaporation: observation of magnetization and its relaxation at low temperature, J. Phys. Chem. B 110 (2006) 15234–15243.
[13] S.J. Stewart, S.J.A. Figueroa, M.B. Sturla, R.B. Scorzelli, F. García, F.G. Requejo, Magnetic $ZnFe_2O_4$ nanoferrites studied by X-ray magnetic circular dichroism and Mossbauer spectroscopy, Phys. B 389 (2007) 155–158.
[14] J.F. Hochepied, P. Bonville, M.P. Pileni, Nonstoichiometric zinc ferrite nanocrystals: syntheses and unusual magnetic properties, J. Phys. Chem. B 104 (2000) 905–912.
[15] Y. Zhang, J.C. Crittenden, D.W. Hand, D.L. Perram, Fixed-bed photocatalysts for solar decontamination of water, Environ. Sci. Technol. 28 (1994) 435–442.
[16] M. Yokoyama, T. Oku, T. Taniyama, T. Sato, E. Ohta, T. Sato, K. Haneda, S. Itoh, K. Kurahashi, M. Takeda, Intraparticle structure in ultra-fine $ZnFe_2O_4$ particles, Phys. B 213–214 (1995) 251–253.
[17] B.P. Zhang, J.L. Zhang, F. Chen, Preparation and characterization of magnetic TiO_2/$ZnFe_2O_4$ photocatalysts by a sol–gel method, Res. Chem. Intermed. 34 (2008) 375–380.
[18] S.D. Jadhav, P.P. Hankare, R.P. Patil, R. Sasikala, Effect of sintering on photocatalytic degradation of methyl orange using zinc ferrite, Mater. Lett. 65 (2011) 371–373.
[19] G.Y. Zhang, Y.Q. Sun, D.Z. Gao, Y.Y. Xu, Quasi-cube $ZnFe_2O_4$ nanocrystals: hydrothermal synthesis and photocatalytic activity with TiO_2 (Degussa P25) as nanocomposite, Mater. Res. Bull. 45 (2010) 755–760.
[20] S.H. Xu, D.L. Feng, W.F. Shangguan, Preparations and photocatalytic properties of visible-light-active zinc ferrite-doped TiO_2 photocatalyst, J. Phys. Chem. C 113 (2009) 2463–2467.
[21] Y. Hou, X.Y. Li, Q.D. Zhao, X. Quan, G.H. Chen, Electrochemically assisted photocatalytic degradation of 4-chlorophenol by $ZnFe_2O_4$-modified TiO_2 nanotube array electrode under visible light irradiation, Environ. Sci. Technol. 44 (2010) 5098–5103.
[22] J.H. Qu, X. Zhao, Design of BDD–TiO_2 hybrid electrode with P–N function for photoelectrocatalytic degradation of organic contaminants, Environ. Sci. Technol. 42 (2008) 4934–4939.
[23] C. He, Y. Xiong, C.H. Zha, X.M. Wang, X.H. Zhu, Approach to a pulse photoelectrocatalytic process for the degradation of organic pollutants, J. Chem. Technol. Biotechnol. 78 (2003) 717–723.
[24] S. Boumaza, A. Boudjemaa, A. Bouguelia, R. Bouarab, M. Trari, Visible light induced hydrogen evolution on new hetero-system $ZnFe_2O_4$/$SrTiO_3$, Appl. Energ. 87 (2010) 2230–2236.
[25] M. Neamtu, C. Catrinescu, A. Kettrup, Effect of dealumination of iron(III)-exchanged Y zeolites on oxidation of Reactive Yellow 84 azo dye in the presence of hydrogen peroxide, Appl. Catal. B: Environ. 51 (2004) 149–157.
[26] J.M. Joseph, R. Varghese, C.T. Aravindakumar, Photoproduction of hydroxyl radicals from Fe(III)-hydroxy complex: a quantitative assessment, J. Photochem. Photobiol. A: Chem. 146 (2001) 67–73.
[27] B.C. Faust, J.M. Allen, Aqueous-phase photochemical formation of hydroxyl radical in authentic cloudwaters and fogwaters, Environ. Sci. Technol. 27 (1993) 1221–1224.
[28] G.V. Buxton, C.L. Greenstock, W.P. Helman, A.B. Ross, Critical review of rate constants for reactions of hydrated electrons, hydrogen atoms and hydroxyl radicals (•OH/•O^-) in aqueous solution, J. Phys. Chem. Ref. Data 17 (1988) 513–886.
[29] H.J. Lv, L. Ma, P. Zeng, D. Ke, T. Peng, Synthesis of floriated $ZnFe_2O_4$ with porous nanorod structures and its photocatalytic hydrogen production under visible light, J. Mater. Chem. 20 (2010) 3665–3672.
[30] A.J. Elliot, AECL Report 11073, CDG-95-167, AECL Research, Chalk River Laboratories, Chalk River, ON, Canada, 1994.
[31] Y.X. Chen, S.Y. Yang, K. Wang, L.P. Lou, Role of primary active species and TiO_2 surface characteristic in UV-illuminated photodegradation of Acid Orange 7, J. Photochem. Photobiol. A: Chem. 172 (2005) 47–54.
[32] X.Z. Li, C.C. Chen, J.C. Zhao, Mechanism of photodecomposition of H_2O_2 on TiO_2 surfaces under visible light irradiation, Langmuir 17 (2001) 4118–4122.
[33] Y. Mao, C. Schoeneich, K.D. Asmus, Identification of organic acids and other intermediates in oxidative degradation of chlorinated ethanes on titania surfaces en route to mineralization: a combined photocatalytic and radiation chemical study, J. Phys. Chem. 95 (1991) 10080–10089.
[34] L.S. Zhang, K.H. Wong, H.Y. Yip, C. Hu, J.C. Yu, P.K. Wong, Effective photocatalytic disinfection of *E. coli* K-12 using AgBr–Ag–Bi_2WO_6 nanojunction system irradiated by visible light: the role of diffusing hydroxyl radicals, Environ. Sci. Technol. 44 (2010) 1392–1398.
[35] S.T. Martin, A.T. Lee, M.R. Hoffmann, Chemical mechanism of inorganic oxidants in the TiO_2/UV process: increased rates of degradation of chlorinated hydrocarbons, Environ. Sci. Technol. 29 (1995) 2567–2573.
[36] H.Z. Zhao, Y. Sun, L.N. Xu, J.R. Ni, Removal of Acid Orange 7 in simulated wastewater using a three-dimensional electrode reactor: removal mechanisms and dye degradation pathway, Chemosphere 78 (2010) 46–51.
[37] P. Bansal, D. Singh, D. Sud, Photocatalytic degradation of azo dye in aqueous TiO_2 suspension: reaction pathway and identification of intermediates products by LC/MS, Sep. Purif. Technol. 72 (2010) 357–365.
[38] M.F. Hou, F.B. Li, X.M. Liu, X.G. Wang, H.F. Wan, The effect of substituent groups on the reductive degradation of azo dyes by zerovalent iron, J. Hazard. Mater. 145 (2007) 305–314.